Nanoarchitecture of a Two-Dimensional Few-Layer Graphene Oxide/π-Conjugated Polyimide Composite for Enhanced Photocatalytic Performance

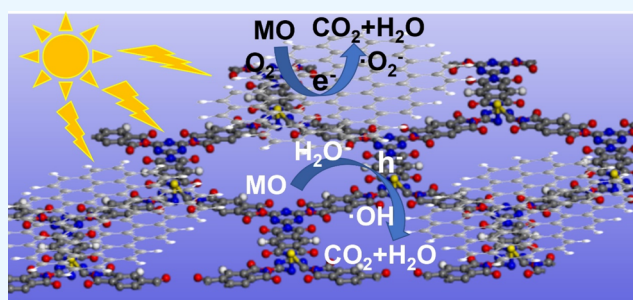Zhiang Luo, Duoping Zhang, Chenghai Ma,* Meitong Zhu, Binhao Li, Laidi Song, and Shiqi Yang

ACCESS | Metrics & More | Article Recommendations | SI Supporting Information

ABSTRACT: A novel two-dimensional graphene oxide/sulfur-doped polyimide (GO/SPI) hybrid polymer photocatalyst was synthesized by a facile ultrasonic chemical method. The characterization results showed that the skeleton structure of SPI was not changed when the few layers of GO were wrapped on the surface. Due to the excellent charge transport characteristics of GO and the strong $\pi-\pi$ stacking interaction between two-dimensional GO and SPI, the photogenerated carrier transport capability of the GO/SPI composites was significantly enhanced compared with that of SPI. The efficient transmission and separation of photogenerated charge carriers significantly improve the photocatalytic degradation of the methyl orange activity of the GO/SPI composite. This work provides a facile and new way for the synthesis of metal-free inorganic–organic composite photocatalysts with high efficiency and low cost.

1. INTRODUCTION

Developing efficient and stable photocatalysts has gradually become one of the most promising strategies to solve the energy shortage and environmental pollution problems by using renewable solar energy. Besides the traditional inorganic semiconductor photocatalyst,[1–3] conjugated organic polymer semiconductor photocatalytic materials are widely favored by many researchers because of their low price, rich source, adjustable structure, and chemical stability. It has been reported that polymer photocatalysts represented by graphitic carbon nitride ($g-C_3N_4$) can photocatalytically decompose water to produce hydrogen and degrade organic pollutants under light irradiation.[4–6] Recently, polyimide (PI) was reported as another kind of conjugated polymer photocatalyst that is functionally comparable to $g-C_3N_4$, which was synthesized by amines and anhydrides using a mild green solid phase thermal polymerization.[7] However, the photocatalytic efficiency of PI is limited due to the inherent characteristics of carrier transitions and photon excitation of conjugated polymers.[8] Since then, many methods, such as structural adjustment,[9] changes of the preparation method,[10,11] element doping,[12,13] and use of a cocatalyst,[14–16] have been used to improve the photogenerated carrier transport and the separation of photogenerated electron–hole pairs to improve the photocatalytic activity of PI. Among them, the enhanced visible light absorption of sulfur-doped polyimide (SPI) improves the photocatalytic activity, but the photocatalytic performance of SPI is still not ideal due to the low efficiency of photogenerated carrier transport and separation. In general,

reducing the conduction band position and narrowing the band gap at the elevated high band position can enhance the absorption of light, but at the same time, it can weaken the reduction and oxidation ability of the photogenerated electrons and holes. Therefore, the cocatalyst can not only maintain the reduction and oxidation capacity of the original catalyst but also rapidly transport and separate photogenerated carriers to improve its photocatalytic performance. Therefore, it is urgent to find a non-metallic oxide cocatalyst with rapid photogenerated charge transfer.

In recent years, graphene oxide (GO) has attracted extensive research interest due to its outstanding advantages such as high mobility of charge transfer carriers, cheap cost, abundant source, and large surface area with abundant active sites,[17–19] Due to its excellent abilities of charge transport and visible light absorption, GO combines with many photocatalysts to effectively improve photocatalytic activity,[20–22] More importantly, the large number of delocalized π bonds in the six-membered ring and the presence of oxygen-containing functional groups at the basal plane and periphery make GO easily bind to conjugated polymers by electrostatic interaction or $\pi-\pi$ stacking.[23] To the best of our knowledge, there are no

reports of GO improving the SPI photocatalytic activity so far. Based on these considerations, the tight binding of GO and SPI is expected to promote the effective separation of photogenerated carriers and the obvious enhancement of light absorption, thus significantly improving its performance in photocatalytic degradation of organic pollutants. Herein, we report a novel inorganic−polymer hybrid photocatalyst [GO/sulfur-doped polyimide (GO/SPI)] prepared via a facile ultrasonic chemical method. The structure, optical, and electronic properties of the hybrid materials are carefully characterized by a variety of spectral techniques. The obtained composites show enhanced photocatalytic activity compared to that of pristine SPI. The effect of the GO content of the samples on the degradation activity of methyl orange (MO) under light irradiation was studied in detail, and a possible photocatalytic mechanism of the GO/SPI composite was also proposed.

2. EXPERIMENTAL SECTION

2.1. Synthesis of the Photocatalyst. Sublimed sulfur (S_4) was purchased from Nanjing Chemical. Melamine (MA) was obtained from Chengdu Kelong Chemical, and pyromellitic dianhydride (PMDA) was the product of Tixiai (Shanghai) Huacheng Industrial Development Co., Ltd. All reagents were directly used as received without further treatment.

GO was synthesized through a commonly used Hummer's method,[20] Typically, under the condition of an ice water bath, 0.5 g of graphite powder and 0.5 g of sodium nitrate were mechanically mixed evenly in 23 mL of concentrated sulfuric acid, and then 3.0 g of potassium permanganate was slowly added. After stirring for 3 h, it was stored at a low temperature for 12 h. After stirring at 35 °C for 40 min, it was heated up to 60 °C, and slowly, 46 mL of ultrapure water was added twice, diluting it to 200 mL of mixed solution after the mixture turns orange. 10 mL of hydrogen peroxide was added, and it was treated with ultrasound for 2 h. After using HCl solution 3 times, a brown−yellow viscous substance was obtained through centrifugation. Finally, GO was obtained by freeze-drying the brown−yellow viscous substance in a Petri dish for 24 h.

π-Conjugated SPI was prepared by a solid phase thermal polymerization as shown in Scheme 1.[12] In detail, a mixture of

Scheme 1. Synthesis of SPI by Polymerization of MA and PMDA at 325 °C
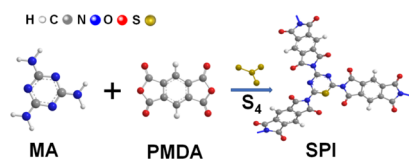
1.0 g of MA, 1.73 g of PMDA, and 0.9 g of sublimed sulfur (S_4) was fully ground and put into a semi-closed system kept at 598 K for 4 h. After cooling to room temperature, the yellow solid powder SPI was obtained.

The GO/SPI composites were synthesized as follows: First, 0.01 g of GO was dispersed in 100 mL of deionized water and ultrasonically dispersed for 1 h. Then, 1.0 g of SPI was poured into the above solution and stirred at 40 °C for 4 h. After 2 h of ultrasonic dispersion and 8 h of vacuum drying at 50°, the composite GO/SPI with a mass percentage of GO of 1 was

obtained and named 1GO/SPI. Similarly, a series of composites were named xGO/SPI, with x representing the mass percentage of GO in the composite (x = 1, 2, 3, 4, and 5%).

2.2. Characterization. The X-ray diffraction (XRD) patterns of the samples were obtained using an X-ray diffractometer with Cu Kα (λ = 1.540562 Å) radiation in the 2θ range from 5 to 70°. Fourier transformed infrared (FTIR) spectra were measured using a Nicolet 6700 spectrometer using the KBr pellet support. Raman experiments were performed using a Horiba confocal LabRAM Aramis spectrometer. The scanning electron microscopy (SEM) images were obtained by using a JSM-6610 system. The transmission electron microscopy (TEM) and high-resolution TEM images were recorded using a JEM-2100 electron microscope. The curves of the pore size distribution and surface area of the samples were inspected by the Barrett−Joyner−Halenda (BJH) method and the Brunauer−Emmet−Teller (BET) method, respectively. UV−vis spectra were tested using a Shimadzu UV-2600 spectrometer, and BaSO$_4$ was used as the reference at room temperature. The photoluminescence (PL) spectrum was performed using an Agilent MY15170004 spectrometer with an excitation wavelength of 350 nm. X-ray photoelectron spectroscopy (XPS) and valence band X-ray photoelectron spectroscopy (VBXPS) were performed using a PHI 5000 Versa Probe X-ray photoelectron spectrometer (a monochromatized Al Kα X-ray radiation).

2.3. Electrochemical Measurements. The photo-electrochemical properties of the prepared samples were tested on a traditional three-electrode system. It was made up of the electrolyte solution (Na$_2$SO$_4$, 0.5 mol L^{-1}, pH = 6.8), a counter electrode (a small piece of platinum), a working electrode, and a reference electrode (an Ag/AgCl electrode). Using the electrophoretic deposition method, the working electrode was fabricated on a fluorine-doped tin oxide (FTO) transparent conductive film glass. Normally, the mixture of 10 mg of I$_2$ and 50 mg of powder sample was dispersed in 50 mL of acetone under sonication for 30 min to obtain the turbid liquid. At the same time, two pieces of FTO glass installed in the electrophoretic deposition apparatus were immersed in the cloudy liquid. The switch was turned on and the voltage kept at 20 V for 5 min. Thus, one piece of the FTO glass with a certain portion of the sample on the conductive face was prepared and dried in air. To reduce the influences of the size of the light irradiation area and the thickness of the prepared sample layer, the light was irradiated on 0.28 cm^2 of the exposure area and the back side (FTO substrate/semiconductor interface). The electro-chemical measurements were carried out using an electrochemical analyzer (CHI-663C, Shanghai Chenhua, China).

2.4. Photocatalytic Performance Measurements. Taking MO as an organic contaminant, an experiment of photocatalytic degradation of MO by the prepared samples was carried out under the condition of visible light, and its photocatalytic performance was evaluated. A light source was achieved by a 300 W xenon lamp (I = 20 A) and a cooling fan. Visible light was obtained by installing a cut-off filter (λ > 420 nm) on the xenon lamp. In each test, 0.2 g of the photocatalyst was put into a three-necked flask containing 100 mL of MO solution (4 mg L^{-1}), and the temperature of the system was kept stable at 25 °C by a constant temperature water bath. To reach the adsorption−desorption equilibrium, the suspension

was magnetically stirred in the dark for 1 h before light irradiation. At 1 h intervals, 4 mL of the suspension was withdrawn and centrifuged to remove most of the catalyst particles. The resulting clear solution was filtered through MCE 0.45 μm, and the absorbance at 464 nm was measured using a UV−visible spectrometer (Mapada UV-1800). The cycling stability of the photocatalyst was measured by five experiments, each with a light duration of 6 h. After the first photocatalytic degradation of MO, the used photocatalyst was filtered and collected from the solution by centrifugation and added back to the reactor for the next run. By analogy, the cycle experiment of photocatalytic degradation of MO was carried out 5 times.

3. RESULTS AND DISCUSSION

3.1. Structure and Morphology Analysis. The XRD patterns of GO, SPI, and the GO/SPI composites are shown in Figure 1. It can be clearly seen from Figure 1 that the
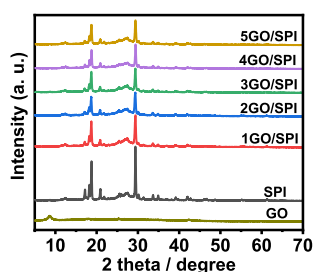
Figure 1. XRD patterns of GO, SPI, and the GO/SPI composite powder samples.

characteristic diffraction peak of SPI appears in the range of 10−30°, which indicates that SPI has been synthesized by in-situ polymerization successfully.[12] The peak located at 19.0° is attributed to the $\pi-\pi$ accumulation of PMDA units,[24] and the distinct peak at 29.6° corresponds to the donor−acceptor interaction in SPI.[25] For GO, the XRD peak at 9.6° is assignable to the interlayer spacing of 0.90 nm, which is consistent with the values reported in the previous literature.[24,25] As Figure S1 shows, after GO was loaded onto SPI, there was no obvious characteristic peak of GO in the XRD pattern of the 2GO/SPI composites, which may be due to the low load and high dispersion of GO. In addition, it can be seen from Figure 1 that the peak positions of the composite did not change compared with the substrate SPI, indicating that the polymeric chain and crystal structure of SPI were not affected by the introduction of GO into SPI. However, it can be seen that the diffraction peak intensity of the GO/SPI composite decreases with the increase of GO content, which may be attributed to the partial peeling of the SPI surface layer under intense stirring and ultrasonic dispersion. Similar phenomena have been reported previously in the literature.[15]

The morphology of the prepared GO, SPI, and 2GO/SPI samples were analyzed by SEM and TEM. Figure 2a shows the SEM image of GO, showing the ultrathin folded layered morphology of GO prepared by Hummer's method. It also can be seen that SPI shows a stacked irregular layered morphology as shown in Figure 2b. From Figure 2c, it can be clearly observed that SPI has been coupled with GO to form a unique ultrathin lamellar structure on the surface of the 2GO/SPI composite. The detailed morphologies of the prepared samples were further studied by TEM. As shown in Figure 2d, GO

demonstrates an ultra-thin structure with multiple layers that are almost transparent. The slight crimping of the nanosheets reduces the surface energy, which is also evidence of ultra-thin thickness. The image of TEM (in Figure 2e) illustrates that SPI consists of layered nanosheets. In the case of the 2GO/SPI hybrid (Figure 2f), it is obviously observed that the surface of SPI is crusted with GO sheets (shown in the yellow arrow), indicating the successful formation of the GO/SPI hetero-structure composite. Sufficient interfacial contact between SPI and GO sheets allows a rapid transfer of the photoexcited charge to the surface, which is conducive to improved photocatalytic activity of SPI. The EDS spectrogram was further used to study the elemental composition, distribution, and content of the prepared photocatalyst. From Figure 2g, it can be clearly seen that the C, N, O, and S elements of the 2GO/SPI composite are evenly distributed in the skeleton, suggesting uniform distribution of GO over the 2D SPI surface.

The characteristic structure and chemical banding of the prepared samples were verified by FTIR spectroscopy. As can be seen from the FTIR spectrum of GO (shown in Figure S2), the peaks in the range of 3700−3000 cm^{-1} are attributed to the adsorbed H$_2$O and the stretching mode of hydroxyl. Also, the peaks located at 3160 and 1400 cm^{-1} are ascribed to the asymmetric stretching vibration absorption of the hydroxyl group and the in-plane bending vibration of O−H in the hydroxyl group, respectively. Moreover, the peaks at 1200 and 1100 cm^{-1} belong to the C−O and C−O−C modes, respectively. These results also fully demonstrate the successful synthesis of GO by the Hummer method.[20,24] In the case of SPI as shown in Figure 3, the peak positions of 1780, 1725, and 725 cm^{-1} are assigned to the stretching vibration and bending vibration of the carbon−oxygen double bond (C=O) in PMDA, respectively. The absorption peaks at 1560 and 1306 cm^{-1} were attributed to the stretching vibration of the C−N bond in the aromatic ring. The absorption peak at 1376 cm^{-1} belongs to the vibration of C−N bonds in the imide ring. The absorption peaks at 1640 and 1157 cm^{-1} are ascribed to the characteristic stretching of carbon−carbon (C−C) bonds in the aromatic benzene ring in the anhydride part.[12] Obviously, the peak positions of the GO/SPI composites are almost unchanged compared with those of SPI, which may be attributed to the low content and high dispersion of GO on SPI. At the same time, the above results also indicate that the introduction of GO does not change the chemical structure of SPI, which is beneficial to improve the photocatalytic stability of the GO/SPI composite. To further analyze the structure of the samples, Raman spectra were tested using a Horiba confocal LabRAM Aramis spectrometer. From Figure S3, it can be clearly observed that the Raman spectra of SPI illustrate two strong bands peaks at about 813 and 986 cm^{-1}. In the Raman spectra of GO, it can be see that two typical D peak and G peak were centered at 1342 and 1578 cm^{-1}, respectively.[25] The D peak arises from the heteroatoms or defects in the graphitic lattice, and the G peak corresponds to the stretching mode of crystalline graphitic carbon.[26] Importantly, both the well-documented D and G bands of GO appeared in the Raman spectra of the GO/SPI composites, by which it turns out that GO was actually introduced into SPI.

XPS is used to identify the elements' states of the samples as a proficient and powerful technique. The binding energies of all elements were calibrated by the C 1s peak (284.6 eV) as a reference, which was attributed to carbon contamination or the sp^2-hybridized carbon atoms.[27] As shown in Figure 4a, the C
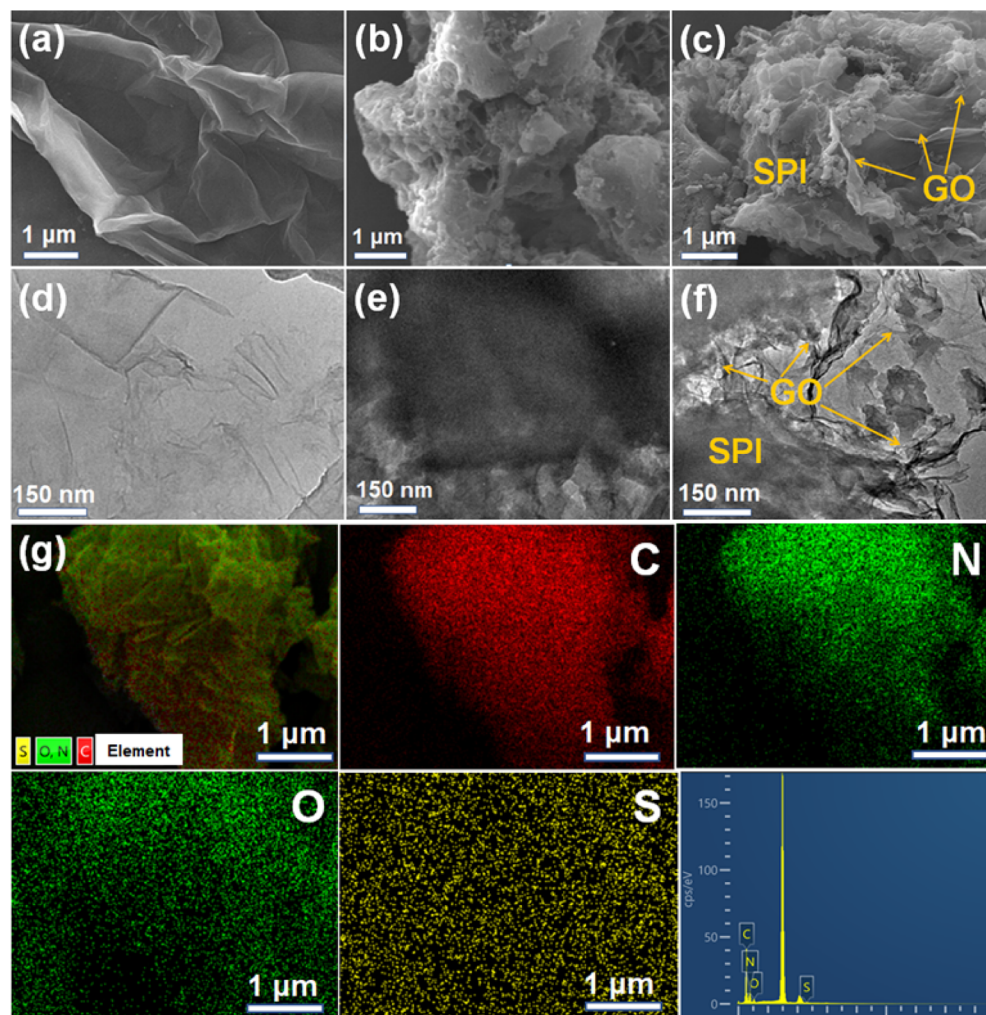
Figure 2. Images of SEM (a−c) and TEM (d−f) for GO, SPI, and the 2GO/SPI composite. (g) EDX elemental mappings of C, N, O, and S for the 2GO/SPI sample.
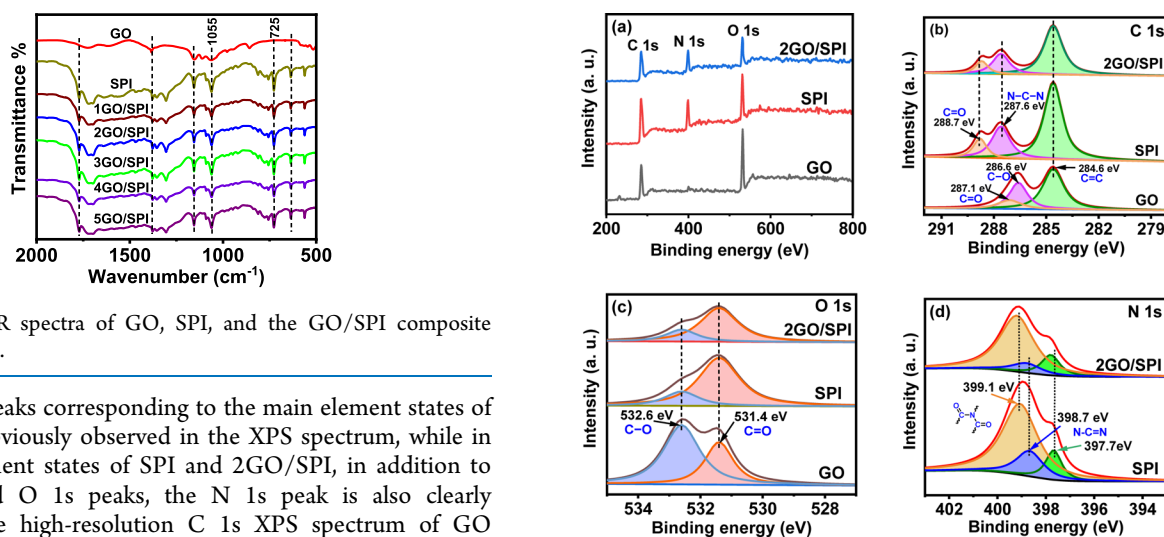
Figure 3. FT-IR spectra of GO, SPI, and the GO/SPI composite powder samples.

1s and O 1s peaks corresponding to the main element states of GO can be obviously observed in the XPS spectrum, while in the main element states of SPI and 2GO/SPI, in addition to the C 1s and O 1s peaks, the N 1s peak is also clearly displayed. The high-resolution C 1s XPS spectrum of GO displays the signal of C=C bonds formed by sp² carbon at 284.6 eV (Figure 4b). The peaks located at higher binding energies correspond to large amounts of sp³ carbon with different C−O bonding configurations. Such as, the binding energy related to the groups of C−O and C=O are located at about 286.6 and 287.1 eV, respectively.[28,29] The C 1s XPS spectra of SPI and the 2GO/SPI composite are shown in

Figure 4. (a) XPS survey, (b) C 1s and (c) O 1s XPS spectra of SPI, GO, and the 2GO/SPI composite. (d) N 1s XPS spectra of GO, SPI, and the 2GO/SPI composite.

Figure 4b. Except for the peak at 284.6 eV, the peaks centered at 287.6 and 288.7 eV could be assigned to the N−C−N bond

and the C=O bond in the triazine rings of SPI, respectively.[27] As shown in Figure 4c, the plotted O 1s binding energy peaks of GO, SPI, and the 2GO/SPI composite samples displayed that two fitted sub-peaks at 531.4 and 532.6 eV are ascribed to the C=O bond and C−O, respectively.[30,31] Through careful observation, it can be found that after the combination of SPI and GO, the ratio of the peak area corresponding to C−O and C=O of the 2GO/SPI composite slightly increases compared with that of SPI. This also proves that SPI is indeed integrated with GO. The N 1s XPS spectra of SPI and the 2GO/SPI composite can be seen in Figure 4d. The N 1s peak located at ∼397.7 eV belongs to the sp²-bonded N in the triazine rings (N−C=N) of SPI. However, the peaks at the binding energies of 398.7 and 399.1 eV are derived from the splitting of the peak of N atoms in the five-membered imide ring of PI after doping sulfur into the triazine ring of PI.[32] Moreover, the binding energies of N 1s peaks of the 2GO/SPI sample are higher than that of SPI, which may be caused by the strong interaction between a few layers of GO and π-conjugated SPI. This strong interaction is conducive to the construction of a dense contact interface between GO and SPI, thus promoting the rapid transmission of light-generated charges.

The BET analysis was performed to verify the surface properties of the SPI and 2GO/SPI composite samples. The specific surface area and porosity were determined using the N₂ adsorption/desorption and BJH tests. According to the IUPAC classification, the SPI and 2GO/SPI composite adsorption/desorption curve could be classified as type IV[33] as shown in Figure 5a, indicating that both SPI and the 2GO/
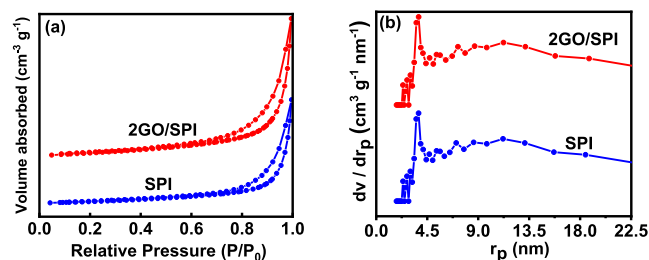
Figure 5. (a) BET surface area isotherms. (b) BJH plot for pore size distribution of SPI and the 2GO/SPI composites.

SPI composites have some mesoporous pores. The BET surface areas of SPI and the 2GO/SPI composite were found to be 6.69 and 12.39 m² g⁻¹, respectively. The specific surface area of the 2GO/SPI composite was significantly higher than that of SPI, leading to the increase of active sites in photocatalytic reactions. As can be seen clearly from Figure 5b, SPI and the 2GO/SPI composite manifest a pore size distribution confined in the range of 2−20 nm with a prominent sharp peak near 3.6 nm, indicating the mesoporous characteristic of SPI and 2GO/SPI, which also would provide rich active sites for photocatalytic reaction, consequently resulting in a high photocatalytic activity.

3.2. Optical Properties. The light response properties of GO, SPI, and the GO/SPI composites were studied by UV−visible spectroscopy. As shown in Figure 6a, the visible light absorption of the GO/SPI composite in the range of 400−800 nm gradually increases with the increase of GO content, which may arise from the generation of new localized electronic states (surface states) within the band gap of SPI.[34] On closer inspection, it is found that the absorption band edge is blue-
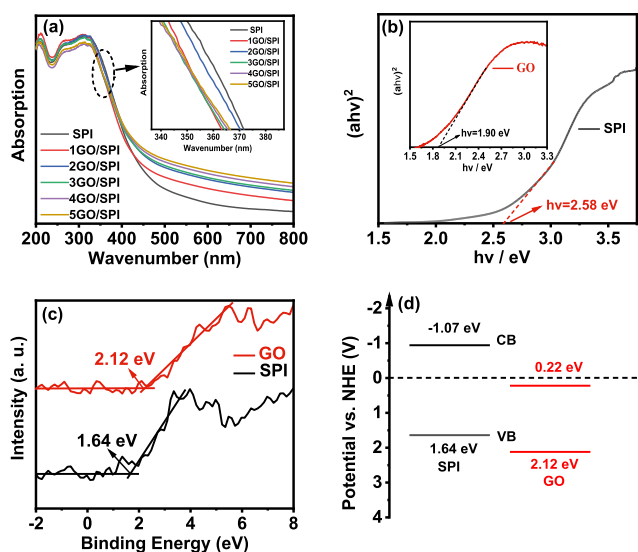
Figure 6. (a) UV−vis diffuse reflectance spectroscopy spectra of the as-prepared pure SPI and the GO/SPI composites. (b) Corresponding plots of $(\alpha h\nu)^2$ vs $h\nu$. (c) VBXPS spectra. (d) Schematic illustration of band structures for SPI and GO.

shifted in the wavelength range of about 340−380, which may be attributed to the quantum size effect caused by the GO ultra-thin nanosheets.[35] In addition, the band gap of the photocatalyst can be evaluated by the Kubelka−Munk function equation, $\alpha h\nu = A(h\nu - E_g)^{1/2}$.[27] As shown in Figure 6b, the band gaps of SPI and GO samples are about 2.58 and 1.90 eV, respectively, by extrapolating the linear region of absorbance squared versus energy. Moreover, the VBXPS spectra of SPI and GO samples illustrated that the energy levels of the valence band (VB) in SPI and GO are approximately 1.64 and 2.12 eV, respectively, as shown in Figure 6c. Thus, the conduction band (E_{CB}) potentials are −1.07 and 0.22 eV for SPI and GO versus NHE estimated by the equation $E_{CB} = E_{VB} - E_g$.[36] Based on these results, the band structures of SPI and GO were determined as shown in Figure 6d.

3.3. Photocatalytic Activity and Mechanism. The photocatalytic performances of the as-prepared SPI and GO/SPI composites were evaluated by the photocatalytic degradation of MO upon visible light illumination. As shown in Figure 7a, the blank test confirmed that the photolysis of methyl orange was negligible. At the same time, the ability of photocatalytic degradation of MO is also very low in the presence of only GO. As we expected, the addition of GO increased the photocatalytic activity of SPI. Interestingly, the GO content has a huge impact on the photocatalytic performances of the GO/SPI composites. The photocatalytic activities of the GO/SPI composite also gradually improved with the increase of GO content, and the degradation rate of MO was 97% when GO loading was up to 2%, achieving the best catalytic performance. The introduction of GO significantly enhanced the activity of SPI in the photocatalytic degradation of MO, which may be attributed to the increased surface area, enhanced visible light absorption intensity, and improved separation efficiency of photogenerated electron−hole pairs. However, a further increase of GO content led to a decrease of photocatalytic degradation efficiency of MO. This may be due to the excessive GO shielding the photoadsorption and inhibiting the production of SPI photogenerated carriers. In addition, the high content of GO tends to form
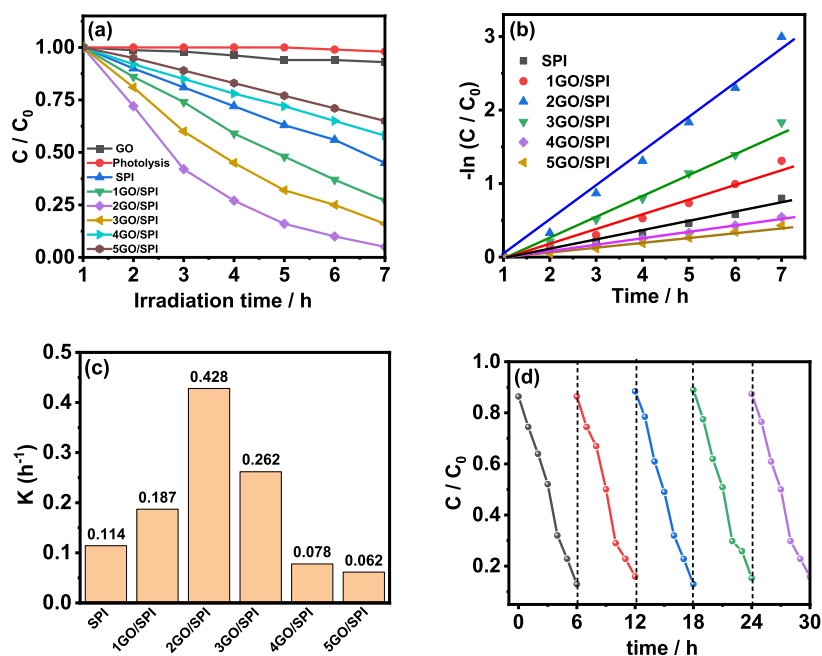
Figure 7. (a) Photocatalytic activities of the MO degradation on GO, SPI, and GO/SPI with different GO contents under visible light irradiation. (b) Kinetic constants of MO degradation with different systems. (c) The calculated corresponding k of different systems. (d) Cycling runs for the photodegradation of MO in the presence of the 2GO/SPI composite sample.

agglomeration points on the surface of SPI, which causes the overlapping of delocalized π bonds in GO to bind photo-generated electrons, leading to the reduction of photocatalytic activity.

Moreover, the reaction kinetics for the MO degradation over SPI and the GO/SPI composite were studied and are shown in Figure 7b,c. It can be clearly seen that the degradation of MO by the GO/SPI composite follows pseudo-first-order kinetics. The apparent rate constant K of the optimized 2GO/SPI is 0.4280 min^{-1}, about 3.75 times that of the bare SPI (0.1141 min^{-1}). This result further confirmed that the GO/SPI composite had a good photocatalytic performance for MO degradation, which may be ascribed to the improved charge carrier separation of the GO/SPI composite and the consequent higher photocatalytic efficiency. In addition, cyclic stability is another important factor to evaluate the performance of a photocatalyst. As shown in Figure 7d, the degradation activity of MO by the 2GO/SPI composite photocatalyst did not decrease significantly after five cycles. Such excellent cyclic stability may be due to the strong interaction and dense contact interface between two-dimensional GO and SPI. To further demonstrate the photocatalyst property, the photocatalytic 2,4-dichlorophenol degradation activities of the prepared samples were tested under visible light. As shown in Figure S4, the blank test confirmed that the photolysis of 2,4-dichlorophenol was negligible. At the same time, the ability of photocatalytic degradation of 2,4-dichlorophenol is also very low in the presence of only GO. Interestingly, the photocatalytic activities of the GO/SPI composite samples also gradually improved with the increase of GO content, and the degradation 2,4-dichlorophenol rate of 2GO/SPI achieved the best catalytic performance. However, the further increase of GO content led to a decrease of photocatalytic degradation efficiency of 2,4-dichlorophenol. In conclusion, the photocatalytic degradation activity of 2,4-dichlorophenol of the GO/SPI composite is indeed signifi-

cantly enhanced compared with that of SPI. Furthermore, GO/SPI showed better photocatalytic 2,4-dichlorophenol degradation activity than that reported in the literature.[26] In addition, we have prepared pristine PI with different mass percentages of GO samples and tested their photocatalytic activity of MO degradation. As shown in Figure S5, it can be clearly seen that the photocatalytic MO degradation activities of most GO/PI composites are significantly enhanced compared with that of pristine PI. However, the photocatalytic degradation activity of the GO/PI composites is lower than that of the GO/SPI composites. This indicates that sulfur doping effectively enhanced visible light absorption of SPI, thus improving its photocatalytic activity.

To explore the mechanism of photocatalytic degradation of MO by the GO/SPI composite semiconductor materials, the PL of the samples was analyzed. Since fluorescence emission results from the recombination of photogenerated electrons and holes, the capture, transfer, separation, and lifetime of photogenerated electrons and holes can be revealed by PL. As shown in Figure 8, it can be clearly seen that the PL spectrum of SPI displays the main emission peak at about 480 nm corresponding to 2.58 eV, which is consistent with the estimated band gap of UV−vis (Figure 6b). This shows that
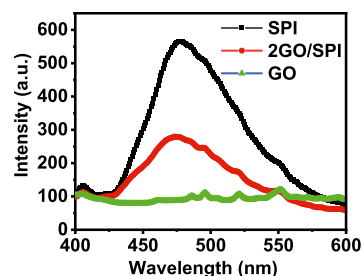
Figure 8. Comparison of photoluminescence spectra of the SPI, 2GO/SPI, and GO samples.
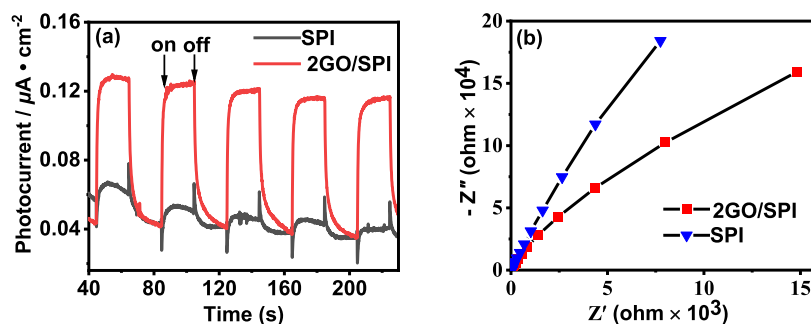
Figure 9. (a) Transient photocurrent response and (b) Nyquist plots of EIS for SPI and 2GO/SPI samples in a 0. 5 M Na_2SO_4 aqueous solution.

the strong emission peak caused by the band−band PL phenomenon with the energy of light is approximately equal to the band gap energy of SPI. It has been previously reported[37] that the band−band PL signal is ascribed to excitonic PL due to transitions of $n-\pi*$ electrons including lone pair electrons of N atoms in SPI. Interestingly, the PL intensity of 2GO/SPI decreased obviously relative to SPI after loading fewer layers of GO nanosheets, indicating that the separation efficiency of photogenerated electron−hole pairs was significantly improved. The improvement of the efficiency of photogenerated carrier separation is mainly due to the photogenerated electrons from the VB to the CB transmitted to GO through the dense contact interface between GO and SPI, which effectively hinders the direct recombination of photogenerated electrons and holes. This is also mainly attributed to the excellent electron conduction ability of GO as an electron acceptor material and the two-dimensional π-conjugate structure in the GO/SPI composite.[38]

To further verify that the loading of GO can improve the separation and migration ability of the electron−hole pair of SPI, the electrochemical properties of SPI and 2GO/SPI composite photocatalysts were studied using transient photo-current and electrochemical impedance spectroscopy (EIS).[39,40] Figure 9a shows that both the SPI and 2GO/SPI light-responsive photocatalysts have a fast and consistent photocurrent response performance. It is noteworthy that the photocurrent density of the GO/SPI composite is about 1.12 μA cm^{-2}, which is about 2.2 times that of bare SPI (0.47 μA cm^{-2}). Specifically, the photocurrent curve of SPI samples is low, and the photocurrent intensity decreases significantly with the increase of time. This may be caused by the delay of charge transmission, the high recombination rate of photogenerated electrons and holes, and the accumulation of charge at the interface due to the carrier transmission characteristics of SPI itself. Interestingly, after the combination with GO, the photocurrent curve of the 2GO/SPI sample is significantly higher than that of SPI, and the photocurrent intensity of the 2GO/SPI sample does not weaken significantly with the increase of time. This indicates that the excellent charge transport performance of GO and the close contact interface between GO and SPI enable the photogenerated electrons to be transferred to the catalyst surface in time, effectively reducing the accumulation of photogenerated charges at the interface and the recombination of photogenerated electron−hole pairs. It further shows that the higher photocurrent pulse effect of 2GO/SPI is conducive to promoting the separation and migration of photogenerated electrons and holes at the interface, thereby reducing the amount of surface charge accumulation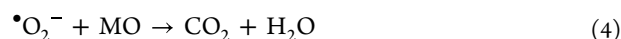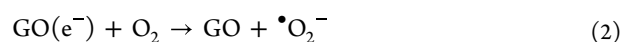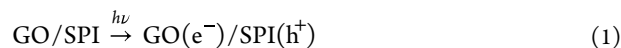 and showing better photocatalytic activity. In addition, Figure 9b shows the resistance changes of bare SPI and 2GO/SPI electrodes. It can be clearly seen that the GO/SPI composite has a smaller arc radius, indicating that its photogenerated electron−hole pair has a higher migration rate and a smaller electron transfer resistance. These results confirm that the introduction of GO is beneficial to the charge transfer in the GO/SPI photocatalytic system, thus reducing the recombination of photogenerated carriers. Therefore, the improved photocatalytic activity of the composite sample may be mainly attributed to the superconductivity of GO and the close contact interface between GO and SPI.
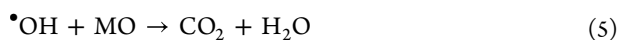
Based on the above results, a possible photocatalytic mechanism to enhance the activity and stability of the GO/SPI composite was proposed, as shown in Figure 10. Under full
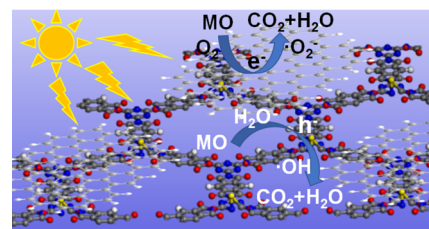
Figure 10. Schematic of the photogenerated charge carrier's separation and transfer in the GO/SPI composite under visible light irradiation.

amplitude light, SPI is excited to produce photogenerated electron (e−)/hole (h+) pairs. Due to the super conductivity of GO and the close contact interface between GO and SPI, the photogenerated charge is rapidly transferred to the surface of the GO/SPI composite to capture oxygen molecules (O_2) and form superoxide radicals ($^\bullet O_2^-$).[41] At the same time, the hole reacts with water to produce hydroxyl radicals ($^\bullet OH$).[42] As the active species of the photocatalytic reaction, both $^\bullet O_2^-$ and $^\bullet OH$ can easily oxidize MO to small inorganic molecules such as CO_2 and H_2O.[43,44] Thus, an effective photocatalytic process was formed, and MO degradation proceeded smoothly. The main reaction steps of the mechanism of photocatalytic degradation of MO under full-amplitude light are summarized by the following eqs 1−5.

$$GO/SPI \xrightarrow{h\nu} GO(e^-)/SPI(h^+) \tag{1}$$

$$GO(e^-) + O_2 \rightarrow GO + {}^\bullet O_2^- \tag{2}$$

$$SPI(h^+) + H_2O \rightarrow SPI + {}^\bullet OH \tag{3}$$

$${}^\bullet O_2^- + MO \rightarrow CO_2 + H_2O \tag{4}$$

$$\bullet OH + MO \rightarrow CO_2 + H_2O \tag{5}$$

4. CONCLUSIONS

In summary, we adopt a facile ultrasonic chemical method to successfully prepare a series of two-dimensional GO/SPI hybrid polymer photocatalysts. Compared with pure SPI, a small amount of GO can effectively increase the specific surface area and light absorption of GO/SPI composites. In particular, the strong charge transport capacity of GO and the dense contact interface formed by the conjugated $\pi-\pi$ strong interaction between two-dimensional GO and SPI greatly improve the separation and transport efficiency of photo-generated electron—hole pairs, leading to a significant enhancement of the photocatalytic degradation activity of MO under solar light irradiation. This work displays a facile new way to synthesize highly efficient inorganic—organic composite photocatalysts. Also, the inexpensive metal-free GO/SPI composites with high photocatalytic activity can find potential applications in water purification.

ASSOCIATED CONTENT

Ⓢ Supporting Information

The Supporting Information is available free of charge at https://pubs.acs.org/doi/10.1021/acsomega.2c07010.

> XRD patterns and FT-IR spectra of pure GO, SPI, and the 2GO/SPI composite powder samples; Raman spectra of GO, SPI, and the GO/SPI composites; photocatalytic activities of 2,4-dichlorophenol degradation on GO, SPI, and GO/SPI with different GO contents under visible light irradiation; and photocatalytic activities of MO degradation on PI and GO/PI composites under visible light irradiation (PDF)

AUTHOR INFORMATION

Corresponding Author

Chenghai Ma — *School of Chemical Engineering, Qinghai University, Xining 810016, China;* ⓞ orcid.org/0000-0002-4965-3024; Email: chmaqhu@126.com

Authors

Zhiang Luo — *School of Chemical Engineering, Qinghai University, Xining 810016, China*

Duoping Zhang — *School of Chemical Engineering, Qinghai University, Xining 810016, China*

Meitong Zhu — *School of Chemical Engineering, Qinghai University, Xining 810016, China*

Binhao Li — *School of Chemical Engineering, Qinghai University, Xining 810016, China*

Laidi Song — *School of Chemical Engineering, Qinghai University, Xining 810016, China*

Shiqi Yang — *School of Chemical Engineering, Qinghai University, Xining 810016, China*

Complete contact information is available at:
https://pubs.acs.org/10.1021/acsomega.2c07010

Notes

The authors declare no competing financial interest.

REFERENCES

(1) Fujishima, A.; Honda, K. Electrochemical Photolysis of Water at a Semiconductor Electrode. *Nature* **1972**, *238*, 37−38.

(2) Ni, M.; Leung, M. K. H.; Leung, D. Y. C.; Sumathy, K. A Review and Recent Developments in Photocatalytic Water-Splitting Using TiO2 for Hydrogen Production. *Renew. Sustain. Energy Rev.* **2007**, *11*, 401−425.

(3) Zou, Z.; Ye, J.; Sayama, K.; Arakawa, H. Direct Splitting of Water under Visible Light Irradiation with an Oxide Semiconductor Photocatalyst. *Nature* **2001**, *414*, 625−627.

(4) Wang, X.; Maeda, K.; Thomas, A.; Takanabe, K.; Xin, G.; Carlsson, J. M.; Domen, K.; Antonietti, M. A Metal-Free Polymeric Photocatalyst for Hydrogen Production from Water under Visible Light. *Nat. Mater.* **2009**, *8*, 76−80.

(5) Stegbauer, L.; Schwinghammer, K.; Lotsch, B. v. A Hydrazone-Based Covalent Organic Framework for Photocatalytic Hydrogen Production. *Chem. Sci.* **2014**, *5*, 2789−2793.

(6) Pan, C.; Xu, J.; Wang, Y.; Li, D.; Zhu, Y. Dramatic Activity of C3N4/BiPO4 Photocatalyst with Core/Shell Structure Formed by Self-Assembly. *Adv. Funct. Mater.* **2012**, *22*, 1518−1524.

(7) Chu, S.; Wang, Y.; Guo, Y.; Zhou, P.; Yu, H.; Luo, L.; Kong, F.; Zou, Z. Facile Green Synthesis of Crystalline Polyimide Photocatalyst for Hydrogen Generation from Water. *J. Mater. Chem.* **2012**, *22*, 15519−15521.

(8) Wan, S.; Gándara, F.; Asano, A.; Furukawa, H.; Saeki, A.; Dey, S. K.; Liao, L.; Ambrogio, M. W.; Botros, Y. Y.; Duan, X.; Seki, S.; Stoddart, J. F.; Yaghi, O. M. Covalent Organic Frameworks with High Charge Carrier Mobility. *Chem. Mater.* **2011**, *23*, 4094−4097.

(9) Chu, S.; Wang, Y.; Guo, Y.; Feng, J.; Wang, C.; Luo, W.; Fan, X.; Zou, Z. Band Structure Engineering of Carbon Nitride: In Search of a Polymer Photocatalyst with High Photooxidation Property. *ACS Catal.* **2013**, *3*, 912−919.

(10) Zhao, C.; Xiong, C.; Liu, X.; Qiao, M.; Li, Z.; Yuan, T.; Wang, J.; Qu, Y.; Wang, X. Q.; Zhou, F.; Xu, Q.; Wang, S.; Chen, M.; Wang, W.; Li, Y.; Yao, T.; Wu, Y.; Li, Y. Unraveling the Enzyme-like Activity of Heterogeneous Single Atom Catalyst. *Chem. Commun.* **2019**, *55*, 2285−2288.

(11) Zhou, J.; Lei, Y.; Ma, C.; Lv, W.; Li, N.; Wang, Y.; Xu, H.; Zou, Z. A (001) dominated conjugated polymer with high-performance of hydrogen evolution under solar light irradiation. *Chem. Commun.* **2017**, *53*, 10536−10539.

(12) Wang, C.; Guo, Y.; Yang, Y.; Chu, S.; Zhou, C.; Wang, Y.; Zou, Z. Sulfur-Doped Polyimide Photocatalyst with Enhanced Photo-catalytic Activity under Visible Light Irradiation. *ACS Appl. Mater. Interfaces* **2014**, *6*, 4321−4328.

(13) Yang, J.; Chu, S.; Guo, Y.; Luo, L.; Kong, F.; Wang, Y.; Zou, Z. Hyperbranched Polymeric N-Oxide: A Novel Kind of Metal-Free Photocatalyst. *Chem. Commun.* **2012**, *48*, 3533−3535.

(14) Li, J. Y.; Jiang, X.; Lin, L.; Zhou, J. J.; Xu, G. S.; Yuan, Y. P. Improving the Photocatalytic Performance of Polyimide by Constructing an Inorganic-Organic Hybrid ZnO-Polyimide Core—Shell Structure. *J. Mol. Catal. A: Chem.* **2015**, *406*, 46−50.

(15) Ma, C.; Zhu, H.; Zhou, J.; Cui, Z.; Liu, T.; Wang, Y.; Wang, Y.; Zou, Z. Confinement Effect of Monolayer MoS2 Quantum Dots on Conjugated Polyimide and Promotion of Solar-Driven Photocatalytic Hydrogen Generation. *Dalton Trans.* **2017**, *46*, 3877−3886.

(16) Ma, C.; Zhou, J.; Zhu, H.; Yang, W.; Liu, J.; Wang, Y.; Zou, Z. Constructing a High-Efficiency MoO3/Polyimide Hybrid Photo-catalyst Based on Strong Interfacial Interaction. *ACS Appl. Mater. Interfaces* **2015**, *7*, 14628−14637.

(17) Xiang, Q.; Yu, J.; Jaroniec, M. Graphene-Based Semiconductor Photocatalysts. *Chem. Soc. Rev.* **2012**, *41*, 782−796.

(18) Iwase, A.; Ng, Y. H.; Ishiguro, Y.; Kudo, A.; Amal, R. Reduced Graphene Oxide as a Solid-State Electron Mediator in Z-Scheme Photocatalytic Water Splitting under Visible Light. *J. Am. Chem. Soc.* **2011**, *133*, 11054−11057.

(19) Zhang, P.; Song, T.; Wang, T.; Zeng, H. Plasmonic Cu Nanoparticle on Reduced Graphene Oxide Nanosheet Support: An Efficient Photocatalyst for Improvement of near-Infrared Photocatalytic H2 Evolution. *Appl. Catal., B* **2018**, *225*, 172−179.

(20) Liao, G.; Chen, S.; Quan, X.; Yu, H.; Zhao, H. Graphene Oxide Modified G-C3N4 Hybrid with Enhanced Photocatalytic Capability under Visible Light Irradiation. *J. Mater. Chem.* **2012**, *22*, 2721−2726.

(21) Zhu, M.; Chen, P.; Liu, M. Graphene Oxide Enwrapped Ag/AgX (X = Br, Cl) Nanocomposite as a Highly Efficient Visible-Light Plasmonic Photocatalyst. *ACS Nano* **2011**, *5*, 4529−4536.

(22) Wang, H.; Zou, L.; Shan, Y.; Wang, X. Ternary GO/Ag3PO4/AgBr Composite as an Efficient Visible-Light-Driven Photocatalyst. *Mater. Res. Bull.* **2018**, *97*, 189−194.

(23) Chen, D.; Wang, K.; Hong, W.; Zong, R.; Yao, W.; Zhu, Y. Visible Light Photoactivity Enhancement via CuTCPP Hybridized G-C3N4 Nanocomposite. *Appl. Catal., B* **2015**, *166−167*, 366−373.

(24) Yeh, T. F.; Syu, J. M.; Cheng, C.; Chang, T. H.; Teng, H. Graphite Oxide as a Photocatalyst for Hydrogen Production from Water. *Adv. Funct. Mater.* **2010**, *20*, 2255−2262.

(25) Xiang, Q.; Yu, J.; Jaroniec, M. Preparation and Enhanced Visible-Light Photocatalytic H2- Production Activity of Graphene/C3N4 Composites. *J. Phys. Chem. C* **2011**, *115*, 7355−7363.

(26) Gong, Y.; Yang, B.; Zhang, H.; Zhao, X.; Zhu, C. Graphene Oxide Enwrapped Polyimide Composites with Efficient Photocatalytic Activity for 2,4-Dichlorophenol Degradation under Visible Light Irradiation. *Mater. Res. Bull.* **2019**, *112*, 115−123.

(27) Hu, Y.; Hao, X.; Cui, Z.; Zhou, J.; Chu, S.; Wang, Y.; Zou, Z. Enhanced Photocarrier Separation in Conjugated Polymer Engineered CdS for Direct Z-Scheme Photocatalytic Hydrogen Evolution. *Appl. Catal., B* **2020**, *260*, 118131.

(28) Wang, Y.; Shao, Y.; Matson, D. W.; Li, J.; Lin, Y. Nitrogen-Doped Graphene and Its Application in Electrochemical Biosensing. *ACS Nano* **2010**, *4*, 1790−1798.

(29) Chang, Y.; Han, G.; Yuan, J.; Fu, D.; Liu, F.; Li, S. Using Hydroxylamine as a Reducer to Prepare N-Doped Graphene Hydrogels Used in High-Performance Energy Storage. *J. Power Sources* **2013**, *238*, 492−500.

(30) Zhu, M.; Yu, S.; Ge, R.; Feng, L.; Yu, Y.; Li, Y.; Li, W. Cobalt Oxide Supported on Phosphorus-Doped g-C3N4 as an Efficient Electrocatalyst for Oxygen Evolution Reaction. *ACS Appl. Energy Mater.* **2019**, *2*, 4718−4729.

(31) Fan, X.; Wang, T.; Gao, B.; Gong, H.; Xue, H.; Guo, H.; Song, L.; Xia, W.; Huang, X.; He, J. Preparation of the TiO2/Graphic Carbon Nitride Core-Shell Array as a Photoanode for Efficient Photoelectrochemical Water Splitting. *Langmuir* **2016**, *32*, 13322−13332.

(32) Chu, S.; Wang, Y.; Wang, C.; Yang, J.; Zou, Z. Bandgap Modulation of Polyimide Photocatalyst for Optimum H2 Production Activity under Visible Light Irradiation. *Int. J. Hydrogen Energy* **2013**, *38*, 10768−10772.

(33) Sun, Y.; Jiang, J.; Liu, Y.; Wu, S.; Zou, J. A Facile One-Pot Preparation of Co3O4/g-C3N4 Heterojunctions with Excellent Electrocatalytic Activity for the Detection of Environmental Phenolic Hormones. *Appl. Surf. Sci.* **2018**, *430*, 362−370.

(34) Kisch, H. Semiconductor Photocatalysis–Mechanistic and Synthetic Aspects. *Angew. Chem., Int. Ed. Engl.* **2013**, *52*, 812−847.

(35) Doolen, R.; Laitinen, R.; Parsapour, F.; Kelley, D. F. Trap State Dynamics in MoS2 Nanoclusters. *J. Phys. Chem. B* **1998**, *102*, 3906−3911.

(36) Jia, X.; Tahir, M.; Pan, L.; Huang, Z. F.; Zhang, X.; Wang, L.; Zou, J. J. Direct Z-Scheme Composite of CdS and Oxygen-Defected CdWO4: An Efficient Visible-Light-Driven Photocatalyst for Hydrogen Evolution. *Appl. Catal., B* **2016**, *198*, 154−161.

(37) Khabashesku, V. N.; Zimmerman, J. L.; Margrave, J. L. Powder Synthesis and Characterization of Amorphous Carbon Nitride. *Chem. Mater.* **2000**, *12*, 3264−3270.

(38) Geim, A. K. Graphene: Status and Prospects. *Science* **2009**, *324*, 1530−1534.

(39) Guiyun, Y.; Hu, F.; Cheng, W.; Han, Z.; Liu, C.; Dai, Y. Zncual-Ldh/Bi2moo6 Nanocomposites with Improved Visible Light-Driven Photocatalytic Degradation. *Wuli Huaxue Xuebao* **2020**, *36*, 1911016.

(40) Shen, R.; He, K.; Zhang, A.; Li, N.; Ng, Y. H.; Zhang, P.; Hu, J.; Li, X. In-Situ Construction of Metallic Ni3C@Ni Core−Shell Cocatalysts over g-C3N4 Nanosheets for Shell-Thickness-Dependent Photocatalytic H2 Production. *Appl. Catal., B* **2021**, *291*, 120104.

(41) Yang, D.; Liu, H.; Zheng, Z.; Yuan, Y.; Zhao, J. C.; Waclawik, E. R.; Ke, X.; Zhu, H. An Efficient Photocatalyst Structure: TiO(2)(B) Nanofibers with a Shell of Anatase Nanocrystals. *J. Am. Chem. Soc.* **2009**, *131*, 17885−17893.

(42) Bie, C.; Yu, H.; Cheng, B.; Ho, W.; Fan, J.; Yu, J. Design, Fabrication, and Mechanism of Nitrogen-Doped Graphene-Based Photocatalyst. *Adv. Mater.* **2021**, *33*, 2003521.

(43) Park, S. J.; Li, K.; Jin, F. L. Synthesis and Characterization of Hyper-Branched Polyimides from 2,4,6-Triaminopyrimidine and Dianhydrides System. *Mater. Chem. Phys.* **2008**, *108*, 214−219.

(44) Wang, W.; Zhao, W.; Zhang, H.; Dou, X.; Shi, H. 2D/2D Step-Scheme α-Fe2O3/Bi2WO6 Photocatalyst with Efficient Charge Transfer for Enhanced Photo-Fenton Catalytic Activity. *Chin. J. Catal.* **2021**, *42*, 97−106.